ACS APPLIED MATERIALS & INTERFACES

Research Article

Cite This: ACS Appl. Mater. Interfaces 2019, 11, 714−721

www.acsami.org

Scalable Engineering of Bulk Porous Si Anodes for High Initial Efficiency and High-Areal-Capacity Lithium-Ion Batteries

Xiang Han,[†] Ziqi Zhang,[†] Guorui Zheng,[‡] Run You,[†] Jianyuan Wang,[†] Cheng Li,[†] Songyan Chen,[*,†] and Yong Yang[*,‡]

[†]Fujian Provincial Key Laboratory of Semiconductors and Applications, Collaborative Innovation Center for Optoelectronic Semiconductors and Efficient Devices, Department of Physics and [‡]State Key Laboratory for Physical Chemistry of Solid Surfaces, Department of Chemistry, Xiamen University, Xiamen 361005, PR China

Supporting Information

ABSTRACT: Nano-Si has been long-hampered in its use for practical lithium battery anodes due to its intrinsic high surface area. To improve the Coulombic efficiency and areal mass loading, we extend the starting materials from nano-Si to photovoltaic waste Si powders (∼1.5 μm). Unique morphology design and interfacial engineering are designed to overcome the particle fracture of micrometer Si. First, we develop a Cu-assisted chemical wet-etching method to prepare micrometer-size bulk-porous Si (MBPS), which provides interconnected porous space to accommodate volume expansion. In addition, a monolithic, multicore, interacting MBPS/carbonized polyacrylonitrile (c-PAN) electrode with strong interfacial Si−N−C is designed to improve the interparticle electrical conductivity during volume expansion and shrinkage. Furthermore, intermediate Si nanocrystals are well-maintained during the lithiation of MBPS, which facilitates the reversibility of lithiation−delithiation process. As a result, the MBPS/c-PAN electrodes exhibit a reversible specific capacity of 2126 mAh g^{-1} with a high initial Coulombic efficiency of 92%. Moreover, even after increasing the capacity loading to 3.4 mAh cm^{-2}, the well-designed electrode shows a capacity retention of 94% in the first 50 cycles at a current density of 0.2 A g^{-1} with deep lithiation and delithiation processes between 0.005 and 2.5 V.

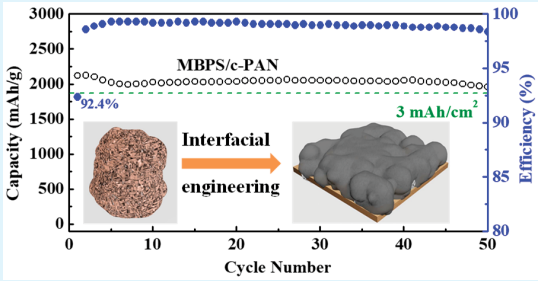

KEYWORDS: *bulk porous Si, wet chemical etching, interfacial Si−N−C engineering, high initial Coulombic efficiency, high areal capacity*

1. INTRODUCTION

Alloy-type anode materials has been considered as potential electrodes to increase the energy density of lithium-ion batteries (LIBs). Among them, Si can deliver a capacity of ∼3579 mAh g^{-1} at room temperature, corresponding to the formation of $Li_{15}Si_4$ alloy. Besides, Si shows multiple advantages)for instance, abundance in earth's crust and low operating potential, <0.4 V versus Li/Li^+). The huge volume changes during the lithiation and delithiation processes, however, causes enormous mechanical stress, the pulverization of Si, loss of the electrical integrity, and continuous reaction with the liquid electrolyte.[1−12] Because the nanostructured materials have a small size that alleviates the lattice stress and shorts the diffusion distance of lithium ions, which can avoid the particle fracture and enhance the kinetics. For example, various silicon nanoparticles, nanowires, nanotubes, nanosheets, and porous structures have been shown big progresses on the cycling performance of LIB anodes.[13−26] The application of Si nanomaterials, however, is impeded by problems them the costly synthesis process and low yield. In addition, the intrinsic large surface area of nano-Si consumes more electrolyte to form solid electrolyte interphase (SEI). As a result, the initial Coulombic efficiency of nano-Si is typically between 65 and 85%, which can not meet the requirements of full-cell applications (90−94%). Furthermore, nano-Si anodes usually deliver low areal capacity (∼1 mAh cm^{-2}) due to its low tap density.

Using micrometer-sized Si (MSi) particles as starting materials can solve the above-mentioned problem. However, the mechanical stability and particle integrity are different from that of nano-Si. Normally, bulk Si particles with a size >150 nm and Si nanowires with a diameter >250 nm have been demonstrated to fracture and break into small nano-Si particles.[27,28] Microsized bulk and porous configurations effectively enable us to solve these problems due to the combination of porous structure and interconnected bulk skeleton. On the one hand, the porous pores can accommodate the volume expansion of silicon, enabling a low expansion ratio of the whole particles. On the other hand, the bulk parts contribute to high mass loading and high areal capacity. Metal-assisted chemical etching (MaCE) with a top-down and wet chemical process has been considered as a scalable technology

Received: September 28, 2018
Accepted: December 10, 2018
Published: December 10, 2018

Downloaded via XIAMEN UNIV on March 14, 2021 at 07:40:45 (UTC).
See https://pubs.acs.org/sharingguidelines for options on how to legitimately share published articles.

 © 2018 American Chemical Society

DOI: 10.1021/acsami.8b16942
ACS Appl. Mater. Interfaces 2019, 11, 714−721

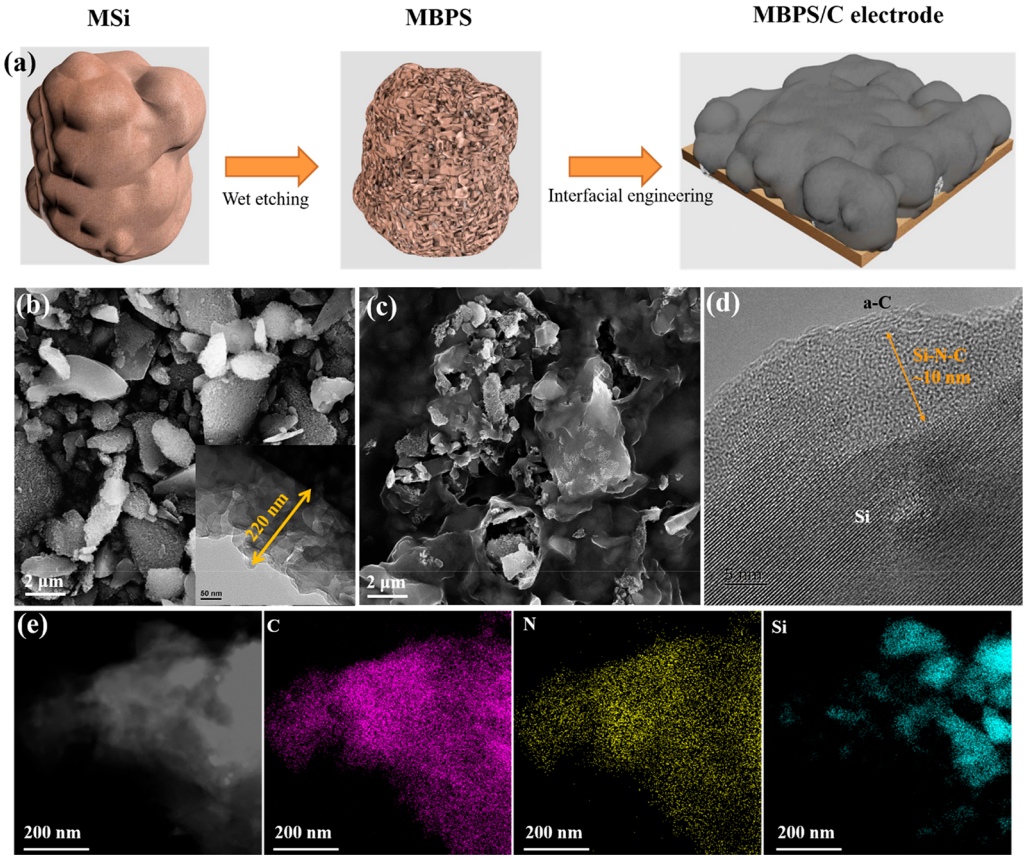

Figure 1. (a) Schematic process of MBPS/c-PAN electrode fabrication. (b) Surface scanning electron microscopy (SEM) image of MBPS powders with uniform shallow pores; the inset transmission electron microscopy (TEM) image shows the porous layer with a thickness of 220 nm. (c) Surface SEM image of the fabricated electrode with MBPS particles embedded in c-PAN. (d) High-resolution TEM image of c-PAN coated MBPS. (e) Dark-field TEM image of c-PAN coated MBPS with corresponding elemental EDS mapping of C, N, and Si.

to synthesis nanostructure Si with mass production. Till date, nano-Si is normally synthesized via MaCE by using of expensive Ag.[29−31] Moreover, to improve the interparticle conductance, especially for high-mass-loading electrodes, new electrode configurations with interfacial engineering between Si and amorphous C needed to be designed.

Herein, we report a scalable route for preparing micron-sized bulk-porous Si (MBPS) prepared by the Cu-assisted wet-etching method using commercially photovoltaic waste Si powders with an average diameter of 1.5 μm. The utilization of the pore penetration and transverse etching mechanisms during the Cu-assisted etching process, a MBPS was fabricated with controlled thickness and porosity. The MBPS offers sufficient inner space to accommodate the volume change, making them serve as efficient integrated host materials. To improve the interparticle conductance between MBPS and C throughout the whole electrode with a high mass loading, we designed a monolithic, cross-linking composite electrode with strong interfacial Si−N−C layer of MBPS/carbonized polyacrylonitrile (c-PAN) electrode (Figure 1a). The c-PAN serving as effective mechanical and electrical linkages with neighboring flakes. Even though some cracks may exist, the strong Si−N−C layer still maintains its electrochemical activity. Furthermore, during repeated charge and discharge processes of MBPS, intermediate nanocrystals were well-maintained instead of totally transformating from the highly crystalline Si to the amorphous Si. The in situ forming Si nanocrystals helps to reduce the activation energy of the phase conversion between a-Si and $LiSi_x$, thus facilitating electrochemical reversibility. We successfully designed a new electrode structure that synergistically enable the mechanical integrity and electrical conductivity. As a result, our MBPS/c-PAN electrodes exhibited a high reversible specific capacity of ∼ 2100 mAh g^{-1} (based on the total mass of MBPS/c-PAN) with a high areal capacity of 3.4−4.5 mAh cm^{-2}. Moreover, high initial Coulombic efficiencies of 88−92% were obtained. The capacity retention of MBPS/c-PAN electrodes after 50 cycles was 92.3% at a deep lithiation−delithiation process of 0.2 A g^{-1} between 0.005 and 2.5 V. Thus, our work proposes an effective novel approach to harness high Coulombic efficiency and high areal capacity anodes with huge volume changes.

2. EXPERIMENTAL SECTION

Synthesis of MBPS. MSi particles with an average size of ∼1.5 μm were used as starting materials. Typically, 5 g of MSi were added to the electrolyte contained 25 mM copper sulfate (CuSO4) and 5 M hydrofluoric acid (HF) at 55 °C and etched for 1, 12, and 24 h. Subsequently, concentrated nitric acid (HNO_3) was used to remove the remaining Cu particles at room temperature for 2 h. The MBPS were washed with alcohol and water several times. Next, the powders were vacuumed dried at 80 °C for 12 h.

Fabrication of MBPS/c-PAN Electrodes. The as-synthesized MBPS particles were ball-milled with PAN (1:1 by weight) in dimethylformamide solvent for 2 h at a speed of 500 r min^{-1} to make slurry. Then the mixed slurry was dropped-cast onto copper disks, which were cut into a diameter of 14 mm and dried in a vacuum oven at 80 °C for 2 h to evaporate the DMF. The as-obtained MBPS/c-

DOI: 10.1021/acsami.8b16942
ACS Appl. Mater. Interfaces 2019, 11, 714−721

PAN electrodes were then transferred to a tube furnace heated to 700 °C at a rate of 5 °C min^{-1} and held for 6 h with a protective Ar/H_2 flow (200 sccm). After annealing, the binder-free MBPS/c-PAN electrodes were stored in a glovebox for cell fabrication.

Characterization. The surface morphology of MBPS/c-PAN was characterized by scanning electron microscopy (SEM, Hitachi S4800). PHI QUANTUM 2000 spectrometer was used to acquire X-ray photoelectron spectroscopy (XPS) spectra. X-ray diffraction (Rigaku Ultima IV) was performed to investigate the crystalline nature of Si and c-PAN. A high accuracy balance (METTLER TOLEDO XS3DU, 1 μg) was used to weigh the mass of MBPS/c-PAN electrodes. Thermal gravimetric analysis (TGA) was tested with a NETZSCH DSC 404 F1 system in air, and the heating rate was 10 °C min^{-1}.

Electrochemical Test. CR2032 coin cells were assembled in a glovebox (Mabrun, H_2O, O_2 of <0.5 ppm) to evaluate electrochemical performance of MBPS/c-PAN with lithium metal as counter-electrodes. The electrolyte in our experiments was 1.0 M $LiPF_6$ in ethylene carbonate (EC)/dimethylcarbonate (DMC)/diethylcarbonate (DEC) = 1:1:1 by weight with 10 wt % fluorinated ethylene carbonate (FEC) additive.[33] A Land CT2001A system was used to record the galvanostatic cycling between 0.005 and 2.5 V at the temperature of 30 °C. After the second delithiation process, the impedance of the cells was tested by applied an alternating current amplitude of 10 mV in a frequency range of 100 kHz and 10 mHz (VersaSTAT MC, America). The cyclic voltammetry data (CV) at scan rates from 0.1 to 1 mV s^{-1} in a voltage range of 0.005−2.5 V.

3. RESULTS AND DISCUSSION

Figure 1b shows the morphology of MBPS particles via a Cu-assisted chemical etching process. Uniform macropores with a narrow distribution of 50−100 nm are obtained on mass-produced particles. A layered porous structure with a thickness of 220 nm is found (inset picture) on the inner bulk Si, indicating the transverse-etching process during pore penetration. The mechanism of MaCE is equivalent to a local Galvani reaction between the Si anode and metal cathode during the dissolution of silicon oxide in HF solution. Regarding this view, the MBPS connected with the Cu particles is continuously etched down to make porous structures. The reaction current density of MBPS etched in $HF/AgNO_3$ or $HF/CuSO_4$ obeys the following equation:

$$J_c = -Nek_c n_s c_{ox} \exp(-E_a/k_B T) \quad (1)$$

wherein J_c is the reactive current density, N is the transferred electron number, e is the elementary charge constant, k_c is the reaction constant, n_s is the electron density at the Metal/MBPS and solution interface, c_{ox} is the interfacial oxidant concentration, E_a is the activation energy, k_B is the Boltzmann constant, and T is the absolute temperature.[32] The catalytic activity of the metal particle is enabled by a decrease in E_a of the cathodic reaction. In view of this, the increased dissolution rate of silicon can be understood by the enhanced cathodic reaction, facilitating by the deposition of Ag/Cu nanoparticles on specific sites. Thanks to the larger redox potential of the Ag/Ag^+ than that of the Cu/Cu^{2+} couples, Ag/Ag^+ couple shows a much faster etching rate. Direct demonstration of pore formation mechanism was performed by time-dependent SEM and transmission electron microscopy (TEM), which is shown in Figure S1. At t = 1 h, no macropores are observed on the MSi while shallow multifold mesopores formed (Figure S1a). In a TEM view, the pore size is ∼20 nm with a depth of ∼ 40 nm. With increased etching time, Cu could traverse etch Si and proceed to internal penetration. As shown in Figure S1b, at t = 12 h, the surface pore diameter shows a large distribution from 50 to 150 nm (Figure S1b). The etching depth is 220 nm with a multiscale layered porous structure, implying the traverse etching process and demonstrating successful formation of multistacked porous flake structures through selective Cu-etching process. At last, at t = 24 h, smooth and uniform surface pores are observed (Figure S1c). The pore size shows a narrow diameter distribution of 160−180 nm. In contrast, for Ag-assisted etched Si, there is a much-higher etching rate. Porous silicon nanowire array was obtained after etching in 0.025 M $AgNO_3$/5 M HF at 55 °C for 2 h, and the thickness is 4.5 μm (Figure S2). The relatively low rate and traverse etching of Cu^{2+}/Cu facilitates us fabricate unique bulk-porous Si structure.

Taking advantage of the bulk porous structure and to enable a high mass loading, MBPS etched for 12 h was chosen as active material. As shown in Figure S3, the MBPS shows a relatively low Brunauer−Emmet−Teller (BET) surface areas of 7.06 m^2 g^{-1}. To further improve the interparticle electrical conductance and to improve the mechanical integrity across the whole electrode, binder-free, monolithic, and cross-linking anodes of c-PAN-coated MBPS were fabricated. The synthesis procedure was described in our previous paper;[33] simple heat treatment process was performed after the PAN/MBPS slurry cast onto the copper foil. Figure 1c shows the surface morphology of c-PAN coated MBPS electrode, and c-PAN acts as conductive, monolithic, cross-linking composite frameworks with MBPS embedded in it. Although some cracks exist, the electrical conductivity should be enhanced on the whole electrode scale. The pore structure was not filled in, and the pore size after carbon coating is the same with that of as-synthesized MBPS. The surface of MBPS skeletons became smooth after non-filling carbon coating was applied. In a high-resolution TEM image (Figure 1d), a condensed Si−N−C layer with a thickness of 10 nm is formed between the crystalline Si and amorphous carbon. This well-designed interphase was expected to improve the interfacial adhesion due to its strong covalent bond nature. Figure 1e shows a dark-field TEM image of a particular MBPS/c-PAN particle, demonstrating successful synthesis of multi-stacked hierarchical porous flake structures through a selective Cu-etching process. Macropores with a size of 50−100 nm are formed over the entire micrometer-size framework. Such high porosity is beneficial for volume expansion and shrinkage during Li ions insertion and extraction, thus maintaining the mechanical integrity. Moreover, the pores can also facilitate liquid electrolyte penetration and enhance the lithium diffusion at the solid−electrolyte interphase. The scanning transmission electron microscopy (STEM) image of MBPS/c-PAN, together with the corresponding elemental mappings of silicon, carbon, and nitrogen, revealing that the MBPS core encapsulated in a uniform nitrogen doped carbon layer. After carbon coating, the specific surface area of the MBPS/c-PAN increases to 26.0 m^2 g^{-1} (Figure S4). Besides to the microporous of MBPS between 50 and 100 nm, mesopores with a diameter of 2−5 nm are detected, an effect caused by the gas spill and defects forming during the carbonization of PAN.

We tested the Fourier transform infrared spectrum of a MBPS/c-PAN sample, and no Si−O stretching bending in plane (1050 cm^{-1}) is found; only a small Si−O stretching bending out plane (1092 cm^{-1}) peak was observed. Instead, series characteristic peaks of Si−N bond at 493, 814, and 1160 cm^{-1} are observed (Figure 2a), corresponding to the Si−N

DOI: 10.1021/acsami.8b16942
ACS Appl. Mater. Interfaces 2019, 11, 714−721

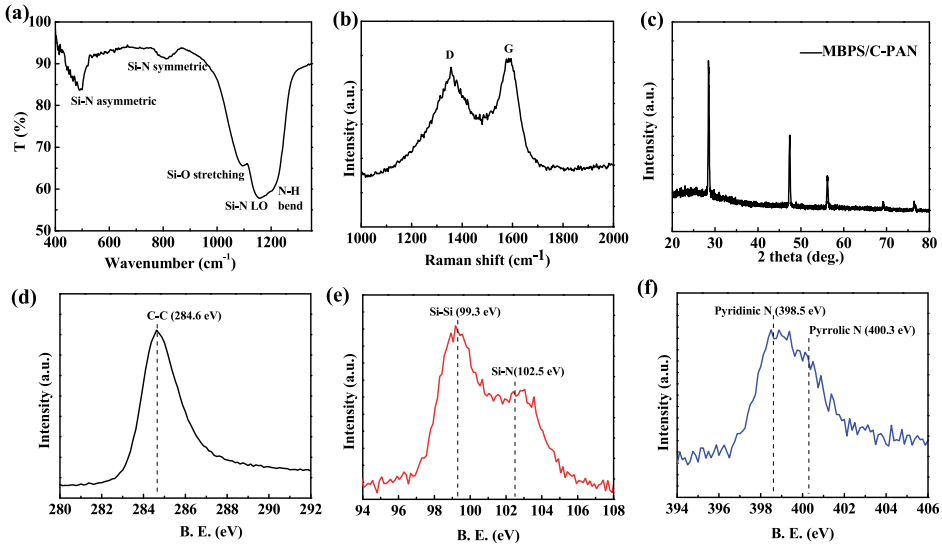

Figure 2. (a) Fourier transform infrared spectrum of MBPS/c-PAN particles. (b) Raman spectra of MBPS/c-PAN. (c) XRD patterns of MBPS/c-PAN. High-resolution XPS spectra of (d) C 1s, (e) Si 2p, and (f) N 1s.

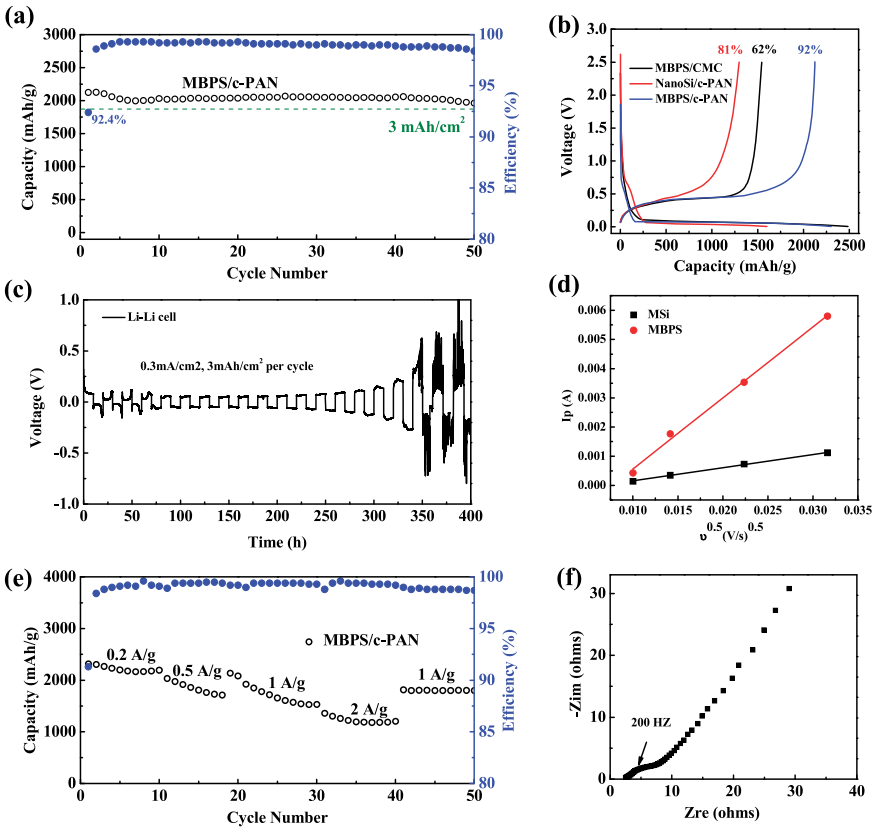

Figure 3. (a) Cycling performance of MBPS/c-PAN at 0.2 A g^{-1} with cutoff voltages ranging from 0.005 to 2.5 V. (b) Initial voltage profiles of MBPS/CMC, nano-Si/c-PAN, and MBPS/c-PAN electrodes at 0.2 A g^{-1} in the potential window 0.005−2.5 V. (c) Li−Li symmetric cell cycled at 0.1 C and 3 mAh cm^{-2}. (d) Plot of the peak current (I_p) vs the square root of the scan rate (ν) and corresponding linear fitting. (e) Rate capacity of MBPS/c-PAN at various currents. (f) EIS measurement of MBPS/c-PAN electrode in a coin cell after 2 charge and discharge processes at 0.2 A g^{-1}.

asymmetric stretching vibrations, Si−N symmetric vibrations, and longitudinal mode (LO) of Si−N stretching vibrations,[34,35] respectively. In addition, N−H (1210 cm^{-1}) bend is also observed. Considering the carbon and nitrogen source are from cyclization PAN, during the heat-treatment process, a conjunct CN polymer parallel, which contained some unreacted −NH/CN triple bonds and a completely unreacted carbon backbone, was found. In Ar plus H_2, the dehydrogenation from the PAN chains is depressed while the surface SiO_2 of MBPS is reduced. The rest of the −NH/CN bands of the c-PAN chain react with the surface fresh Si and form Si−N covalence. Because the N is embedded in pyridinic N and

DOI: 10.1021/acsami.8b16942
ACS Appl. Mater. Interfaces 2019, 11, 714−721

pyrrolic N carbon rings, we call it the interfacial Si−N−C layer, implying the strong adhesion between Si and nitrogen doped carbon; the molecule of reaction product is shown in Figure S5. The Raman spectrum was used to characterize the carbon nature (Figure 2b), and the D band (1356 cm^{-1}) and G band (1592 cm^{-1}) were observed, which are corresponding to the disorder-related phonon mode and delocalized sp^2 π bonds of graphite carbon, respectively. The high value of I_D/I_G for c-PAN corresponded to an amorphous feature of the carbon.[36] We believe the disorders of carbon could enhance lithium ion diffusion and help restrict the volume changes. High-resolution X-ray photoelectron spectroscopy (XPS) was performed to characterize the surface and interfacial valence state of MBPS/c-PAN. The XPS spectra of C 1s confirms carbonized nature of c-PAN, and a main peak at 284.6 eV (Figure 2c) is observed, corresponding to chemical bond energy of graphitic sp^2 carbon with nitrogen doping. Figure 2d shows the high-resolution XPS spectra of Si 2p, besides the main peak located at 99.3 eV (Si 2p), and a clear shadow peak at 102.5 eV is observed, which is correspond to Si−N bond. In the N 1s spectrum of MBPS/c-PAN (Figure 2e), pyridinic N (398.5 eV) and pyrrolic N (400.3 eV) are detected,[37] further confirming the strong Si−N−C interaction. The highly crystalline nature of Si is expected to improve the reversibility of electrochemical reaction. As shown in Figure S6a, the Raman spectrum of MBPS with a main peak at 517.4 cm^{-1} is observed, and the value is lower than that of standard crystalline Si (520.8 cm^{-1}) caused by the surface porous Si. A relatively low full width at half-maximum value of 6.9 cm^{-1} is calculated based on Gauss fitting, corresponding to a highly crystalline state of the porous bulk configuration. In addition, the X-ray diffraction (XRD) patterns of both MSi and MBPS (Figure S6b) exhibit sharp peaks, further confirming its highly crystalline nature. After annealing, the XRD peaks of MBPS/c-PAN (Figure 2c) correspond to the cubic phase of silicon, a broad swell peak around 26.5°, implying the amorphous nature of c-PAN. No crystalline Si−N peak is observed.

The electrochemical performance of MBPS/c-PAN sealed in half cells and paired with lithium foil was measured. All of the capacities are calculated on the total mass of MBPS and c-PAN. Figure 3a shows the cycling stability of MBPS/c-PAN anodes with a current density of 0.2 A g^{-1} with a deep lithiation process between 0.005 and 2.5 V. After annealing, MBPS/c-PAN composites were tested by thermogravimetric analysis (TGA), and the contents of c-PAN and Si are 31 and 69 wt %, respectively (Figure S7). The engineered MBPS/c-PAN shows a capacity retention of 92.3% after 50 cycles. Note that, typically, micrometer-sized Si anodes shows drastic capacity loss during the initial several cycles, caused by the breakdown of the conductive framework. According to the fracture growth mechanism, the surface layer of Si accumulates stress and degrades first. In our case, the surface porous structure is effective to accommodate volume change, and although the bulk Si exhibits a huge volume expansion, the whole particle integrity will be well-maintained. Moreover, the c-PAN not only serves as a coating layer but also forms a wrapping-like monothetic network with strong Si−N−C interaction between Si and C. As a result, a robust electron pathway has built throughout the whole electrode during repeated volume expansion and shrinkage. Even at a high loading to 1.6 mg cm^{-2}, the MBPS/c-PAN still exhibits a high initial capacity of 2125 mAh g^{-1}, corresponding to an areal capacity of >3.4 mAh cm^{-2}. We noticed that the Coulombic efficiency reduced after 30 cycles, and this may attribute to the "dead" lithium of Li deposition and stripping. As we know, Li dendrites grow and react with carbonate-based electrolyte formed SEI (Li_2CO_3 etc.). To detect the SEI growth and its induced polarization voltage in our half cells, we have fabricated Li−Li symmetric cells. The Li deposition and stripping capacity per cycle is 3 mAh cm^{-2} at a C/10 rate, which is the same with that of our half cells. From Figure 3c, we can see the sharp voltages variation that in the first 3 cycles due to the increase of surface area in the dendrite-formation process. After that, the morphology may come to a short stable period in the following 10 cycles; however, due to the high activity between Li metal and carbonate electrolyte, the SEI becomes thicker and induces a large voltage polarization of the Li−Li cell. After 15 cycles, the polarization voltage reached above 0.2 V. Thus, we conclude that the thicker SEI and "dead" Li on Li metal caused the Coulombic efficiency degradation in the half-cell after 30 cycles.

Figure 3b exhibits the first discharge−charge curves of the MBPS/CMC, nano-Si/c-PAN, and MBPS/c-PAN electrodes at 0.2 A g^{-1}. For MBPS/CMC, the initial Coulombic efficiency is only 62%, and the weak hydrogen-bond interaction is not sufficient to hold the mechanical integrity during volume expansion, thus causing irreversible capacity loss. Meanwhile, even strong Si−N−C bonding on the surface of nano-Si, the first Coulombic efficiency increases to 81%. Regardless, the much-higher surface area of nanosize Si (21 m^2 g^{-1}), which normally consume more liquid electrolyte and form SEI in the first cycle. The strong interaction between nano-Si and conductive carbon really helps to eliminate the mesopores of nano-Si and construct the electron pathway during large volume expansion and shrinkage, thus improving the reversibility during cycling. At last, Si−N−C interfacial layer coated on MBPS with relatively small surface area (7.06 m^2 g^{-1}), an extremely high Coulombic efficiency of 92% is achieved. In addition, we have tested the cells with a loading of 2.1 mg cm^{-2} in a voltage range of 0.005−1.5 V (Figure S8). At a loading of 2.1 mg cm^{-2}, the reversible capacity is 2142 mAh g^{-1} (4.5 mAh cm^{-2}) with an initial Coulombic efficiency of 88%. At a high areal capacity loading of 4.5 mAh cm^{-2}, due to a limited time, no capacity fading was observed during the initial 5 cycles. Our MBPS/c-PAN electrodes can deliver high areal capacities with high Coulombic efficiencies, which are among the first-grade level of recent published paper (Table S1). This exceptionally high initial Coulombic efficiency is attributed to the unique porous-bulk structure and interfacial nitrogen engineering. Though the MBPS exhibits a larger surface area, the compact Si−N layer can avoid Li ions consumption by minimizing exposure of MBPS in electrolyte.[38,39] In addition, the strong interfacial adhesion helps maintain the electrical conductivity between Si and a-C during volume expansion and shrinkage, thus improving the electrochemical reversibility. Furthermore, the SiN layer is demonstrated to effectively accommodate the mechanical stress and serve as a support framework to prevent fracture or porous silicon particles from aggregation.[40,41] The high initial Coulombic efficiency and areal capacity are among the best of recent published results (Table S1).

The bulk porous structure design is expected the Li^+ transport from the liquid electrolyte to the active materials. According to the semi-infinite and finite model proposed by Levi and Aurbach, for separate reduction−oxidation reactions, the peak current (I_p) is in direct proportion to the square root

DOI: 10.1021/acsami.8b16942
ACS Appl. Mater. Interfaces 2019, 11, 714−721

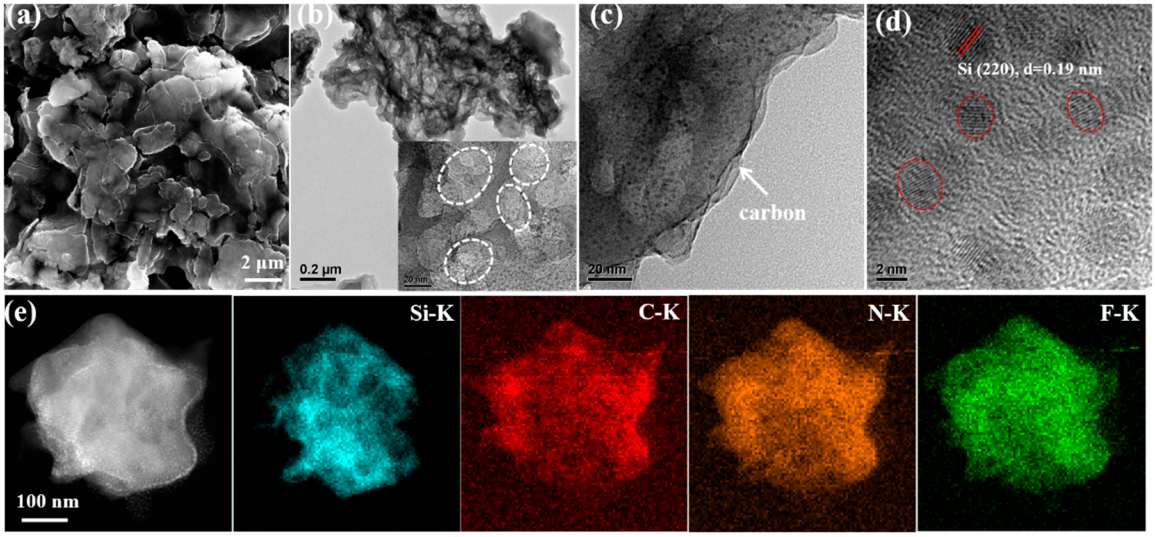

Figure 4. Morphology of MBPS/c-PAN electrode after 20 cycles at a current density of 0.2 A g^{-1} between 0.005 and 2.5 V. (a) SEM image and (b) TEM image; inset is the high-magnification view of the morphology in panels b and c. (b) Cross-edge view. (d) High-resolution TEM view in panel c. (e) Dark-field TEM image V and the EDS elemental mapping of Si, C, N, and F.

of the scan rate (ν), and the I_p of the CV curve can be expressed as:

$$I_p = 2.69 \times 10^5 n^{3/2} A D^{1/2} \nu^{1/2} \Delta C_0 \quad (2)$$

where n is the transferred electron number, A is the reactive area, D is the diffusion coefficient, and ΔC_0 is the Li concentration change.[42] According to this, we tested the CV of MSi/c-PAN and MBPS/c-PAN at different scan rates form 0.1 to 1 mV/s (Figure S9). The diffusion coefficient of MBPS is almost 50 times higher than that of micrometer scale Si (MSi) calculated by the linear fitting results (Figure 3d). The rate performance of MBPS/c-PAN was also tested (Figure 3e) and even increase the current density to 2 A g^{-1}; the electrode still exhibits a capacity of 1205 mA h g^{-1}. As shown in Figure 3f, the EIS measurement of the MBPS electrode shows a small charge-transfer resistance (<10 ohm), further demonstrating the high electrical conductivity across the whole electrode enabled by the monothetic and cross-linked c-PAN.

The structure stability and morphology evolution of MBPS/c-PAN electrodes were characterized by SEM and TEM after 20 cycles. As shown in Figure 4a, although some cracks are observed on the surface of cycled MBPS/c-PAN electrode, the surface c-PAN still shows a cross-linking configuration that bind MBPS. For an individual MBPS/c-PAN particle after 20 cycles (Figure 4b), the integrated particle with fine porous pores are observed with a uniform amorphous coating layer. The original pores are enlarged, and some formed new pores with a diameter of ~20 nm (inset picture) caused by the repeated volume expansion and shrinkage. These results directly demonstrate that the well-designed porous structure is effective to accommodate the large volume change without particle fracture. In addition, the cycled MBPS particles are still hosted by the conductive c-PAN framework through Si−N−C interlayer. Figure 4c shows the cross-section parts of cycled MBPS/c-PAN, a uniform carbon layer is clearly observed on the well maintained MBPS particles. In addition, some dark nanodots with a narrow diameter range are found dispersed in the MBPS framework. In a high-magnification view (Figure 4d), the nanodots turn out to be crystalline Si with a diameter of ~3 nm. The nanodots are found with a d spacing of 0.19 nm calculating from the FFT results, attributing to the (220) plane of cubic Si. This indicates that the electrochemical induced amorphization of Si is not directly transformed from the high-crystalline Si to the amorphous product. In fact, another intermediate phase of nano-Si, is sustained during cycling. Thus, the in situ formed amorphous network may be composed of distributed nanosized Si crystals. This unique structural characteristic can enhance the kinetics and mechanical properties.[43] The Si nanodots may help to enhance the reversibility of lithiation-delithiatoin processes. During delithiation, the existence of a-$LiSi_x$ as well as uniformly Si nanocrystals help to reduce the activation energy or overpotential of the dealloying process from $LiSi_x$ to a-Si.[44] This could contribute to a fast delithiation process, which improves the reversibility of MBPS/C. The Cu-assisted MBPS particle integrity and high Li extraction kinetics contributes to the high Coulombic efficiency.

Elemental distribution information on MBPS/c-PAN electrode after 20 cycles was also detected (Figure 4e). In the dark-field TEM image, the Si nanocrystals could also be observed embedded in the porous Si skeleton. The Si−K mapping clearly exhibits fine porous structure even after repeated volume expansion and shrinkage. It is not surprised that the uniform surface nitrogen-doped carbon is still coated on the porous Si, which further confirms the strong interaction between Si and C. The well-maintained mechanical structure and robust electron pathway synergistically enhances the electrochemical performance of the MBPS/c-PAN electrode. It is interesting that uniform F was detected on the surface of cycled MBPS/c-PAN electrode. The covalent state is calibrated to be LiF by XPS spectrum (Figure S10), and LiF is known as a soft layer to protect a continuous reaction between liquid electrolyte and Si.[45]

4. CONCLUSIONS

In summary, the designed MBPS/c-PAN electrodes show great high initial Columbic efficiency and consistent excellent cycling performance at high mass. First, the interconnect porous structure of MBPS/c-PAN anodes is helpful to accommodate the large volume expansion and mitigate the particle fracture.

DOI: 10.1021/acsami.8b16942
ACS Appl. Mater. Interfaces 2019, 11, 714−721

The MBPS flake has a multistacked structure can avoid the particle pulverization because neighboring pores are integrated by the series walls. In addition, the interfacial Si−N−C layer helps improve the adhesion between MBPS and c-PAN, serving as effective mechanical and electrical linkages with neighboring flakes. Even though some cracks may exist, the strong Si−N−C layer still maintains its electrochemical activity. Furthermore, the in situ forming of intermediate phase such as Si nanocrystals helps to reduce the activation energy of the phase conversion between a-Si and $LiSi_x$, thus facilitating electrochemical reversibility. Different from other nano-Si anodes, the MBPS/c-PAN anode exhibits favorable cycling stability and excellent initial Coulombic efficiency (85−92%) and high areal capacity (3.4−4.5 mAh cm^{-2}). Noticeably, these were accomplished with a scalable Cu-assisted electrochemical etching micrometer-sized Si particle manner.

■ ASSOCIATED CONTENT

Supporting Information

The Supporting Information is available free of charge on the ACS Publications website at DOI: 10.1021/acsami.8b16942.

SEM and TEM images, BET surface area and pore volume distribution, a schematic molecule of the interfacial Si−N−C, Raman spectra and XRD patterns, first charge−discharge profile and cycling performance of MBPS/c-PAN, and cyclic voltammograms (PDF)

■ AUTHOR INFORMATION

Corresponding Authors

*E-mail: sychen@xmu.edu.cn.

*E-mail: yyang@xmu.edu.cn.

ORCID

Ziqi Zhang: 0000-0002-7773-5748

Songyan Chen: 0000-0002-4945-1537

Notes

The authors declare no competing financial interest.

■ ACKNOWLEDGMENTS

We greatly acknowledge all of the financial support from the National Natural Science Foundation of China (grant nos. 61534005, 21233004, and 61474081), the General Armaments Department of China (grant no. 6140721040411), and the Fujian Provincial Department of Education (grant no. JA15651).

■ REFERENCES

(1) Larcher, D.; Beattie, S.; Morcrette, M.; Edstroem, K.; Jumas, J.; Tarascon, J. Recent Findings and Prospects in The Field of Pure Metals as Negative Electrodes for Li-Ion Batteries. *J. Mater. Chem.* **2007**, *17*, 3759−3772.

(2) Takezawa, H.; Ito, S.; Yoshizawa, H.; Abe, T. Comparative Study of Approaches to Achieve Improved Cyclability and High Capacity in A Silicon Suboxide Film Anode for Lithium-Ion Batteries. *Electrochim. Acta* **2017**, *245*, 1005−1009.

(3) Zhang, W. A Review of The Electrochemical Performance of Alloy Anodes for Lithium-Ion Batteries. *J. Power Sources* **2011**, *196*, 13−24.

(4) Obrovac, M.; Christensen, L. Structural Changes in Silicon Anodes during Lithium Insertion/Extraction. *Electrochem. Solid-State Lett.* **2004**, *7*, A93−A96.

(5) Huang, S.; Fan, F.; Li, J.; Zhang, S.; Zhu, T. Stress Generation during Lithiation of High-Capacity Electrode Particles in Lithium Ion Batteries. *Acta Mater.* **2013**, *61*, 4354−4364.

(6) Wu, H.; Chan, G.; Choi, J.; Ryu, I.; Yao, Y.; McDowell, M.; Lee, S. W.; Jackson, A.; Yang, Y.; Hu, L. Stable Cycling of Double-Walled Silicon Nanotube Battery Anodes through Solid-Electrolyte Interphase Control. *Nat. Nanotechnol.* **2012**, *7*, 310−315.

(7) Zhu, B.; Jin, Y.; Tan, Y.; Zong, L.; Hu, Y.; Chen, L.; Zhu, J.; Chen, Y.; Zhang, Q. Scalable Production of Si Nanoparticles Directly from Low Grade Sources for Lithium-Ion Battery Anode. *Nano Lett.* **2015**, *15*, 5750−5754.

(8) Jin, Y.; Zhang, S.; Zhu, B.; Tan, Y.; Hu, X.; Zong, L.; Zhu, J. Simultaneous Purification and Perforation of Low-Grade Si Sources for Lithium-Ion Battery Anode. *Nano Lett.* **2015**, *15*, 7742−7747.

(9) Luo, W.; Chen, X.; Xia, Y.; Chen, M.; Wang, L.; Wang, Q.; Yang, J.; Li, W. Surface and Interface Engineering of Silicon-Based Anode Materials for Lithium-Ion Batteries. *Adv. Energy Mater.* **2017**, *7*, 1701083.

(10) Luo, W.; Wang, Y.; Wang, L.; Jiang, W.; Chou, S. L.; Dou, S. X.; Yang, J.; Liu, H. K. Silicon/Mesoporous Carbon/Crystalline TiO_2 Nanoparticles for Highly Stable Lithium Storage. *ACS Nano* **2016**, *10*, 10524−10532.

(11) Liu, Y.; Tai, Z.; Zhou, T.; Sencadas, V.; Zhang, J.; Zhang, L.; Liu, H. K.; Konstantinov, K.; Guo, Z. An All-Integrated Anode via Interlinked Chemical Bonding between Double-Shelled Yolk-Structured Silicon and Binder for Lithium-Ion Batteries. *Adv. Mater.* **2017**, *29*, 1703028.

(12) Yang, J.; Wang, Y.; Li, W.; Wang, L.; Fan, Y.; Jiang, W.; Liu, H. K.; Luo, W.; Wang, Y.; Kong, B.; et al. Amorphous TiO_2 Shells: A Vital Elastic Buffering Layer on Silicon Nanoparticles for High-Performance and Safe Lithium Storage. *Adv. Mater.* **2017**, *29*, 1700523.

(13) Luo, W.; Wang, Y.; Chou, S.; Xu, Y.; Li, W.; Kong, B.; Yang, J.; Dou, S. X.; Liu, H. K. Critical Thickness of Phenolic Resin-Based Carbon Interfacial Layer for Improving Long Cycling Stability of Silicon Nanoparticle Anodes. *Nano Energy* **2016**, *27*, 255−264.

(14) Yang, J.; Wang, Y. X.; Chou, S. L.; Zhang, R.; Xu, Y.; Fan, J.; Dou, S. X.; Zhang, W.-X.; Kun Liu, H.; Zhao, D.; et al. Yolk-Shell Silicon-Mesoporous Carbon Anode with Compact Solid Electrolyte Interphase Film for Superior Lithium-Ion Batteries. *Nano Energy* **2015**, *18*, 133−142.

(15) Liu, Z.; Guan, D.; Yu, Q.; Xu, L.; Zhuang, Z.; Zhu, T.; Mai, L.; Zhao, D.; Zhou, L. Monodisperse and Homogeneous SiOx/C Microspheres: A Promising High-Capacity and Durable Anode Material for Lithium-Ion Batteries. *Energy Storage Mater.* **2018**, *13*, 112−118.

(16) An, Y.; Fei, H.; Zeng, G.; Ci, L.; Xiong, S.; Feng, J.; Qian, Y. Green, Scalable, and Controllable Fabrication of Nanoporous Silicon from Commercial Alloy Precursors for High-Energy Lithium-Ion Batteries. *ACS Nano* **2018**, *12*, 4993−5002.

(17) Guo, S.; Hu, X.; Hou, Y.; Wen, Z. Tunable Synthesis of Yolk-Shell Porous Silicon@Carbon for Optimizing Si/C-Based Anode of Lithium-Ion Batteries. *ACS Appl. Mater. Interfaces* **2017**, *9*, 42084−42092.

(18) Liu, N.; Wu, H.; McDowell, M.; Yao, Y.; Wang, C.; Cui, Y. A Yolk-Shell Design for Stabilized and Scalable Li-Ion Battery Alloy Anodes. *Nano Lett.* **2012**, *12*, 3315−3321.

(19) Liu, N.; Lu, Z.; Zhao, J.; McDowell, M. T.; Lee, H.; Zhao, W.; Cui, Y. A Pomegranate-Inspired Nanoscale Design for Large-Volume-Change Lithium Battery Anodes. *Nat. Nanotechnol.* **2014**, *9*, 187−192.

(20) Liang, J.; Li, X.; Hou, Z.; Guo, Y.; Zhu, Y.; Qian, Y. Nanoporous Silicon Prepared through Air-Oxidation Demagnesiation of Mg_2Si and Properties of Its Lithium Ion Batteries. *Chem. Commun.* **2015**, *51*, 7230−7233.

(21) Sun, C. F.; Zhu, H.; Okada, M.; Gaskell, K.; Inoue, Y.; Hu, L.; Wang, Y. Interfacial Oxygen Stabilizes Composite Silicon Anodes. *Nano Lett.* **2015**, *15*, 703−708.

(22) Xu, Y.; Zhu, Y.; Han, F.; Luo, C.; Wang, C. 3D Si/C Fiber Paper Electrodes Fabricated Using A Combined Electrospray/Electrospinning Technique for Li-Ion Batteries. *Adv. Energy Mater.* **2015**, *5*, 1400753.

(23) Han, X.; Chen, H.; Liu, J.; Liu, H.; Wang, P.; Huang, K.; Li, C.; Chen, S.; Yang, Y. A Peanut Shell Inspired Scalable Synthesis of Three-Dimensional Carbon Coated Porous Silicon Particles as an Anode for Lithium-Ion Batteries. *Electrochim. Acta* **2015**, *156*, 11−19.
(24) Lv, G.; Zhu, B.; Li, X.; Chen, C.; Li, J.; Jin, Y.; Zhu, J.; Hu, X. Simultaneous Perforation and Doping of Si Nanoparticles for Lithium-Ion Battery Anode. *ACS Appl. Mater. Interfaces* **2017**, *9*, 44452−44457.
(25) Shang, H.; Zuo, Z.; Yu, L.; Wang, F.; He, F.; Li, Y. Low-Temperature Growth of All-Carbon Graphdiyne on A Silicon Anode for High-Performance Lithium-Ion Batteries. *Adv. Mater.* **2018**, *30*, 1801459.
(26) Jung, C. H.; Choi, J.; Kim, W. S.; Hong, S. H. A Nanopore-Embedded Graphitic Carbon Shell on Silicon Anode for High Performance Lithium Ion Batteries. *J. Mater. Chem. A* **2018**, *6*, 8013−8020.
(27) Kim, H.; Seo, M.; Park, M.; Cho, J. A Critical Size of Silicon Nano-Anodes for Lithium Rechargeable Batteries. *Angew. Chem., Int. Ed.* **2010**, *49*, 2146−2149.
(28) Liu, X.; Zheng, H.; Zhong, L.; Huang, S.; Karki, K.; Zhang, L. Q.; Liu, Y.; Kushima, A.; Liang, W. T.; Jiang, W. W.; et al. Anisotropic Swelling and Fracture of Silicon Nanowires during Lithiation. *Nano Lett.* **2011**, *11*, 3312−3318.
(29) Bang, B. M.; Kim, H.; Song, H. K.; Cho, J.; Park, S. Scalable Approach to Multi-Dimensional Bulk Si Anodes *via* Metal-Assisted Chemical Etching. *Energy Environ. Sci.* **2011**, *4*, 5013−5019.
(30) Li, X.; Yan, C.; Wang, J.; Graff, A.; Schweizer, S.; Sprafke, A.; Wehrspohn, R.; Schmidt, O. G. Stable Silicon Anodes for Lithium-Ion Batteries Using Mesoporous Metallurgical Silicon. *Adv. Energy Mater.* **2015**, *5*, 1401556.
(31) Chen, Y.; Liu, L.; Xiong, J.; Yang, T.; Qin, Y.; Yan, C. Porous Si Nanowires from Cheap Metallurgical Silicon Stabilized by a Surface Oxide Layer for Lithium Ion Batteries. *Adv. Funct. Mater.* **2015**, *25*, 6701−6709.
(32) Peng, K. Q.; Hu, J. J.; Yan, Y. J.; Wu, Y.; Fang, H.; Xu, Y.; Zhu, J.; Lee, S. T. Fabrication of Single-Crystalline Silicon Nanowires by Scratching A Silicon Surface with Catalytic Metal Particles. *Adv. Funct. Mater.* **2006**, *16*, 387−394.
(33) Han, X.; Chen, H.; Li, X.; Wang, J.; Li, C.; Chen, S.; Yang, Y. Interfacial Nitrogen Stabilizes Carbon-Coated Mesoporous Silicon Particle Anodes. *J. Mater. Chem. A* **2016**, *4*, 434−442.
(34) Song, C.; Huang, R.; Wang, X.; Guo, Y.; Song, J. Tunable Red Light Emission from a-Si: H/a-SiN_x Multilayers. *Opt. Mater. Express* **2013**, *3*, 664−670.
(35) Torchynska, T.; Polupan, G.; Khomenkova, L.; Slaoui, A. Emitting Modification in Si-rich-SiN_x Films versus Silicon Nitride Compositions. *MRS Commun.* **2017**, *7*, 280−285.
(36) Ferrari, A.; Meyer, J. C.; Scardaci, V.; Casiraghi, C.; Lazzeri, M.; Mauri, F.; Piscanec, S.; Jiang, D.; Novoselov, K. D.; Roth, S.; et al. Raman Spectrum of Graphene and Graphene Layers. *Phys. Rev. Lett.* **2006**, *97*, 187041.
(37) Piper, D.; Yersak, T.; Son, S.; Kim, S.; Kang, C.; Oh, K.; Ban, C.; Dillon, A.; Lee, S. Conformal Coatings of Cyclized-PAN for Mechanically Resilient Si Nano-Composite Anodes. *Adv. Energy Mater.* **2013**, *3*, 697−702.
(38) Wu, C. Y.; Chang, C. C.; Duh, J. G. Silicon Nitride Coated Silicon Thin Film on Three Dimensions Current Collector for Lithium Ion Battery Anode. *J. Power Sources* **2016**, *325*, 64−70.
(39) Weeks, S. L.; Leick, N.; Agarwal, S. Silicon Nitride Encapsulated Silicon Nanocrystals for Lithium Ion Batteries. *Plasma Processes Polym.* **2016**, *13*, 116−123.
(40) Zhang, X. N.; Pan, G. L.; Li, G. R.; Qu, J. Q.; Gao, X. P. Si-Si_3N_4 Composites as Anode Materials for Lithium Ion Batteries. *Solid State Ionics* **2007**, *178*, 1107−1112.
(41) Huang, X.; Zhang, F.; Cao, Y.; Huang, Q. A. Symmetrical Sandwich-Structured SiN/Si/SiN Composite for Lithium-Ion Battery Anode with Improved Cyclability and Rate Capacity. *J. Electrochem. Soc.* **2018**, *165*, A3397−A3402.
(42) Das, S. R.; Majumder, S. B.; Katiyar, R. S. Kinetic Analysis of the Li^+ Ion Intercalation Behavior of Solution Derived Nano-Crystalline Lithium Manganate Thin Films. *J. Power Sources* **2005**, *139*, 261−268.
(43) He, Y.; Zhong, L.; Fan, F.; Wang, C.; Zhu, T.; Mao, S. In Situ Observation of Shear-Driven Amorphization in Silicon Crystals. *Nat. Nanotechnol.* **2016**, *11*, 866−871.
(44) Tang, W.; Liu, Y.; Peng, C.; Hu, M. Y.; Deng, X.; Lin, M.; Loh, K.; Hu, J. Z. Probing Lithium Germanide Phase Evolution and Structural Change in A Germanium-in-Carbon Nanotube Energy Storage System. *J. Am. Chem. Soc.* **2015**, *137*, 2600−2607.
(45) Xu, C.; Lindgren, F.; Philippe, B.; Gorgoi, M.; Bjorefors, F.; Edstrom, K.; Gustafsson, T. Improved Performance of the Silicon Anode for Li-Ion Batteries: Understanding the Surface Modification Mechanism of Fluoroethylene Carbonate as An Effective Electrolyte Additive. *Chem. Mater.* **2015**, *27*, 2591−2599.

DOI: 10.1021/acsami.8b16942
ACS Appl. Mater. Interfaces 2019, 11, 714−721